



Shultis, J., Waugh, DW., Toigo, AD., Newman, CE., Teanby, N. A., & Sharkey, J. (2022). Winter Weakening of Titan's Stratospheric Polar Vortices. *Planetary Science Journal*, [73].
<https://doi.org/10.3847/PSJ/ac5ea1>

Publisher's PDF, also known as Version of record

License (if available):
CC BY

Link to published version (if available):
[10.3847/PSJ/ac5ea1](https://doi.org/10.3847/PSJ/ac5ea1)

[Link to publication record in Explore Bristol Research](#)
PDF-document

This is the final published version of the article (version of record). It first appeared online via American Astronomical Society at <https://doi.org/10.3847/PSJ/ac5ea1>. Please refer to any applicable terms of use of the publisher.

University of Bristol - Explore Bristol Research

General rights

This document is made available in accordance with publisher policies. Please cite only the published version using the reference above. Full terms of use are available:
<http://www.bristol.ac.uk/red/research-policy/pure/user-guides/ebr-terms/>



Winter Weakening of Titan's Stratospheric Polar Vortices

J. Shultis¹, D. W. Waugh¹, A. D. Toigo², C. E. Newman³, N. A. Teanby⁴, and J. Sharkey⁴

¹Department of Earth and Planetary Sciences, Johns Hopkins University, Baltimore, MD 21210, USA; jshulti1@jhu.edu

²Johns Hopkins Applied Physics Laboratory, MD, USA

³Aeolis Research, USA

⁴School of Earth Sciences, University of Bristol, Bristol, UK

Received 2021 November 30; revised 2022 March 14; accepted 2022 March 15; published 2022 April 4

Abstract

Polar vortices are a prominent feature in Titan's stratosphere. The Cassini mission has provided a detailed view of the breakdown of the northern polar vortex and formation of the southern vortex, but the mission did not observe the full annual cycle of the evolution of the vortices. Here we use a TitanWRF general circulation model simulation of an entire Titan year to examine the full annual cycle of the polar vortices. The simulation reveals a winter weakening of the vortices, with a clear minimum in polar potential vorticity and midlatitude zonal winds between winter solstice and spring equinox. The simulation also produces the observed postfall equinox cooling followed by rapid warming in the upper stratosphere. This warming is due to strong descent and adiabatic heating, which also leads to the formation of an annular potential vorticity structure. The seasonal evolution of the polar vortices is very similar in the two hemispheres, with only small quantitative differences that are much smaller than the seasonal variations, which can be related to Titan's orbital eccentricity. This suggests that any differences between observations of the northern hemisphere vortex in late northern winter and the southern hemisphere vortex in early winter are likely due to the different observation times with respect to solstice, rather than fundamental differences in the polar vortices.

Unified Astronomy Thesaurus concepts: [Atmospheric science \(116\)](#); [Planetary atmospheres \(1244\)](#); [Atmospheric circulation \(112\)](#); [Titan \(2186\)](#); [Saturnian satellites \(1427\)](#); [Stratosphere \(1640\)](#)

1. Introduction

A prominent feature of Titan's stratosphere is the presence of polar vortices. Similar to Earth's stratosphere, these polar vortices are characterized by a cold pole and strong circumpolar winds and exist during winter but not summer (e.g., Achterberg et al. 2008; Flasar & Achterberg 2009). Another similarity is the composition within the vortices, with enhanced concentrations of trace gases with a mesospheric source (e.g., Plumb et al. 2002; Vinatier et al. 2015, 2020; Coustenis et al. 2018; Teanby et al. 2019) and clouds (e.g., Tritscher et al. 2021; Anderson et al. 2018; West et al. 2016; Le Mouélic et al. 2018) within both Earth's and Titan's polar vortices. The polar vortices appear to sit at the edge of a meridional overturning circulation, which, during winter, consists of a single cell with ascent at summer high latitudes and descent at winter high latitudes. The strong circumpolar winds form in the winter hemisphere at the edge of the descending branch of this overturning circulation, and the strong polar descent leads to enhanced concentrations of trace gases within the vortex (e.g., Teanby et al. 2017, 2019; Coustenis et al. 2018; Sylvestre et al. 2020; Vinatier et al. 2010, 2015, 2020).

The Cassini mission provided a detailed view of the thermal structure and composition of Titan's polar regions (e.g., Coustenis et al. 2018; Sylvestre et al. 2018; Teanby et al. 2019; Mathé et al. 2020). These observations show an increase in temperature and decrease in trace gas concentrations in the northern polar region for a planetocentric solar longitude, L_S , of

$293^\circ\text{--}360^\circ$ (or 0°), indicating the breakdown of the northern polar vortex (e.g., Teanby et al. 2008; Achterberg et al. 2011). They also show the formation of the southern vortex between southern fall equinox and winter solstice ($L_S \sim 0^\circ\text{--}93^\circ$). There is rapid cooling of the southern polar upper stratosphere/mesosphere after fall equinox, which is followed by warming before winter solstice (Teanby et al. 2017, 2019; Vinatier et al. 2015, 2020). The rapid mesospheric cooling has been hypothesized to be related to enhanced emissions due to the trace gas enrichment associated with postequinox descent and cooling (Teanby et al. 2008, 2017; Achterberg et al. 2008, 2011; Vinatier et al. 2020).

The structure and evolution of the polar vortices are further determined by the zonal winds and potential vorticity (PV), which can be calculated from the observed temperatures assuming gradient wind balance (e.g., Sharkey et al. 2021). Calculations based on Cassini measurements show strong zonal winds ($\sim 200\text{ m s}^{-1}$) and large PV in the northern hemisphere during the first half of the mission (late winter to spring equinox), which decay to weak westerlies and PV in the second half, with the reverse transition in the southern hemisphere (weak winds and PV that increase after $L_S = 0^\circ$) (Sharkey et al. 2021). This analysis also shows an annular PV structure, with a ring of large PV encircling a local minimum over the winter pole.

However, Cassini observations only cover the $L_S = 293^\circ\text{--}90^\circ$ period, and the full annual cycle of the vortices is not observed by Cassini. Wind measurements in the upper stratosphere to thermosphere are also available from Atacama Large Millimeter/submillimeter Array (ALMA) observations (Lellouch et al. 2019) and Cordiner et al. (2020) but these still only have limited seasonal coverage. This raises several questions, including how does the vortex structure change



Original content from this work may be used under the terms of the [Creative Commons Attribution 4.0 licence](#). Any further distribution of this work must maintain attribution to the author(s) and the title of the work, journal citation and DOI.

between early and late winter (a period not observed in either hemisphere)? Are the differences in Cassini observations for the northern and southern polar vortices due to hemispheric differences in the vortex structure, or are they a result of different seasonal periods being compared (late northern winter versus the very start of southern winter)? What mechanisms control the vortex structure and evolution?

To answer these questions, we use a TitanWRF general circulation model simulation covering an entire Titan year (Newman et al. 2011). We examine the full annual evolution of the northern and southern polar vortices in this simulation, including an analysis of the vortex structure in terms of zonal winds and PV (which can only be approximated from temperature observations) and analysis of the relationship between the vortex and the mean meridional circulation (MMC; which cannot be directly observed and has to be inferred from observations of trace gases). While several other studies have examined stratospheric fields from three-dimensional general circulation models and compared them with observations (e.g., Newman et al. 2011; Lebonnois et al. 2012; Lora et al. 2015), these studies have not focused on the structure or seasonal evolution of the polar vortices.

The model simulations and observations are described in the next section, and then in Section 3, we compare the simulated fields with observed fields and fields derived from observations. In Section 4 we examine the annual cycle of the vortices, hemispheric differences, and mechanisms for the simulated structures. In the final section, we summarize our conclusions.

2. Methods

2.1. TitanWRF

We examine a simulation from the TitanWRF model, which is the Titan-specific implementation of the planetWRF model (Richardson et al. 2007; Newman et al. 2011). The simulation that we analyze is the TitanWRF v2 standard resolution run from Newman et al. (2011). This configuration has 5.625° longitudinal by 5° latitudinal horizontal resolution, 54 vertical levels extending up to a rigid model top at 0.02 Pa, with the highest model layer centered at around 0.2 Pa (approximately 430 km), and has a latitude-dependent polar filter poleward of 45° , which prevents numerical instabilities as the spacing between longitude grid points decreases toward the poles. At the surface, angular momentum is exchanged via drag between the atmosphere and surface, while heat is exchanged via a 12 layer subsurface scheme that assumes the deepest layer temperature (at 5.53 m depth) is constant at 94 K. There is Rayleigh drag in the top four model layers, with horizontal winds relaxed to their zonal-mean values on timescales that decrease from 6 to 1 Titan sol toward the top of the model.

The simulation has no explicit horizontal diffusion, and vertical mixing is parameterized using a scheme adapted from that of Hong & Pan (1996). This scheme parameterizes local mixing (in all regions) by diffusion and nonlocal mixing (only inside the boundary layer) by the addition of a term that depends on atmospheric stability conditions. A two-stream radiative transfer scheme is used to calculate visible and IR heating rates, with gas and haze optical properties found using the modified McKay et al. (1989) scheme.

The simulation used in this work assumes uniform surface properties, including flat topography, with the albedo, density, specific heat capacity, and thermal inertia of the surface equal

to 0.32 , 800 kg m^{-3} , $1400 \text{ J kg}^{-1} \text{ K}^{-1}$, and $335 \text{ J m}^2 \text{ s}^{-1/2} \text{ K}^{-1}$, respectively. The acceleration due to gravity, the specific heat capacity at constant pressure, and the gas constant are held constant throughout the atmosphere at 1.352 m s^{-2} , $1044 \text{ J K}^{-1} \text{ kg}^{-1}$, and $290 \text{ J kg}^{-1} \text{ K}^{-1}$, respectively. This simulation does not include a radiatively or chemically active methane cycle, although one was added to the TitanWRF model in a later version of the model than the one which produced this simulation. That version of the model including a methane cycle was used for analysis within the troposphere, and the stratosphere was not investigated there (Newman et al. 2016). The lack of a methane cycle in the model should not change the conclusions herein, as the intent for this work was to use a basic state for investigation of the polar vortex annual cycle and dynamics.

As shown in Newman et al. (2011), this TitanWRF simulation generates a circulation that reproduces the main observed features of Titan’s circulation, including strong stratospheric superrotation, realistically strong latitudinal temperature gradients, and zonal wind jets.

In this work, we focus on an examination of the temperature (T), zonal wind (U), and PV, from year 76 of the TitanWRF simulation presented in Newman et al. (2011). Titan’s slow rotation and long radiative time constants require a long, multiyear “spin-up” period, in particular to accelerate the superrotation to its quasi-equilibrium state. This particular simulation took 69 Titan years to reach a steady state before a regular seasonal cycle developed.

2.2. Observations

In the next section, we compare the model results with T, U, and PV derived from Cassini Composite Infrared Spectrometer (CIRS) observations by Sharkey et al. (2021). The derivation of these fields from observations is described in detail in Sharkey et al. (2021) and is only briefly summarized here. They retrieve temperatures from spectral observations using the method of Sharkey et al. (2020). The zonal-mean zonal winds are then calculated using the gradient wind equation, which relates the vertical gradient of the zonal wind to the meridional gradient of temperature, and these are combined with the retrieved temperature to calculate PV using the equation from Sharkey et al. (2021):

$$\text{PV} = -g \frac{\partial \theta}{\partial p} (f + \zeta_\theta), \quad (1)$$

where g is the acceleration due to gravity, f is the Coriolis parameter, ζ_θ is the vertical component of relative vorticity calculated on isentropic surfaces, θ is the potential temperature, and p is the pressure. PV is the product of the absolute vorticity ($f + \zeta_\theta$) and stratification, a form of static stability ($-g \partial \theta / \partial p$). The solution for the gradient wind balance is undefined as the equator is approached, and thus results for zonal wind and PV within a zone around the equator were not computed. The derived fields are computed on a 1° latitude grid with a varying number of vertical levels depending on the variable, with 148 vertical levels between 10 and 10^{-5} hPa for U and 95 vertical levels between 9 and 10^{-4} hPa for PV.

3. Model Evaluation

We begin by evaluating how well the TitanWRF simulation reproduces the observed structure and the evolution of Titan’s

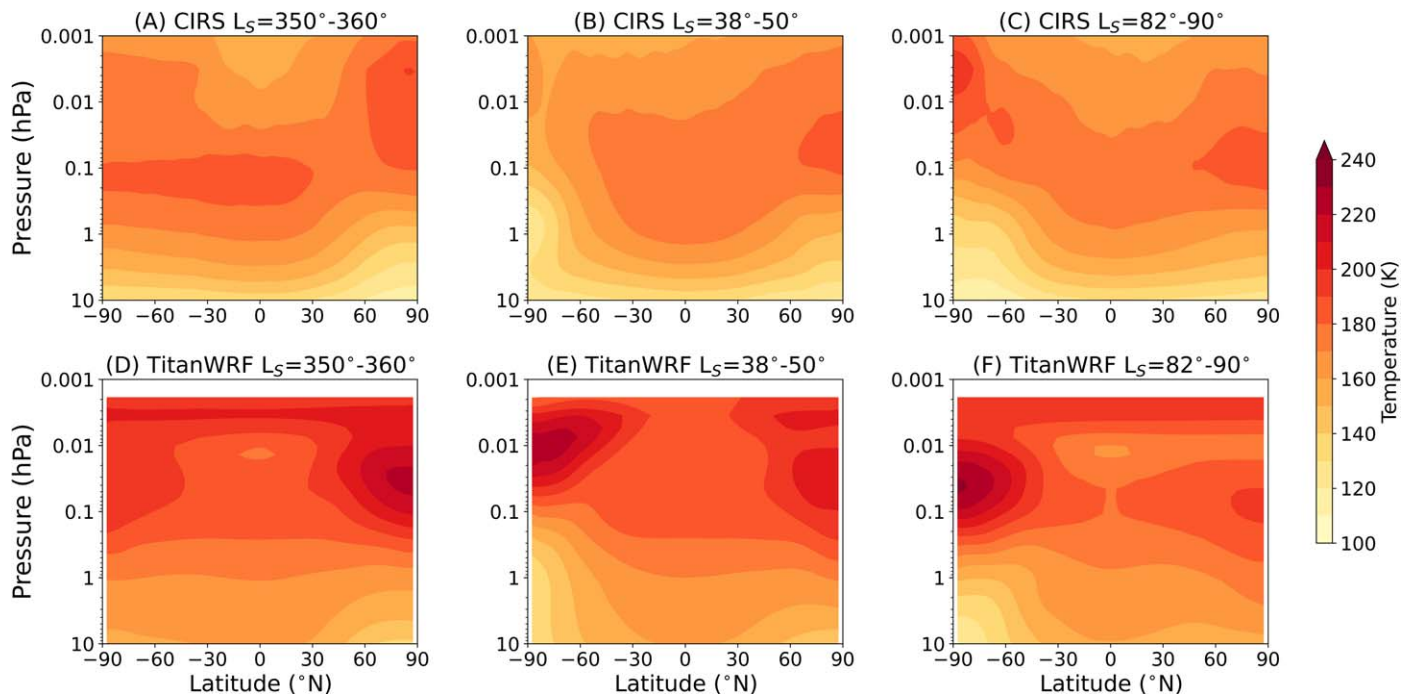


Figure 1. Zonally averaged temperature from CIRS (A–C) and TitanWRF (D–F) at southern fall equinox (left), southern midfall (middle), and southern winter solstice (right). Values are only shown here and in the following figures for the 10 hPa–0.001 hPa range to focus on behavior in the stratosphere and mesosphere.

polar vortices. As discussed above, our main comparison is with the fields derived from Cassini CIRS observations by Sharkey et al. (2021). For our comparison, we select three times when Cassini observations provide near pole-to-pole coverage: $L_S = 350^\circ\text{--}360^\circ$, $38^\circ\text{--}50^\circ$, and $82^\circ\text{--}90^\circ$ (see Figure 1 of Sharkey et al. 2021), and average the TitanWRF output over the same time periods. We focus on the zonal-mean distributions, as both observations (Sharkey et al. 2020) and the simulation show only weak zonal variations.

We first consider the temperature distribution. CIRS observations show that the winter pole in the upper stratosphere/mesosphere (<0.01 hPa) is warmer than that at lower latitudes, while the winter pole is colder in the lower to middle stratosphere (>1 hPa). This occurs for both late northern winter (Figure 1(A)) and early southern winter (Figure 1(C)). Here, winter is defined as the time between the winter solstice and spring equinox ($L_S = 90^\circ\text{--}180^\circ$ in the southern hemisphere (SH) and $L_S = 270^\circ\text{--}0^\circ$ in the northern hemisphere (NH)), and summer is defined as the time between the summer solstice and the autumnal equinox ($L_S = 270^\circ\text{--}0^\circ$ in the SH and $L_S = 90^\circ\text{--}180^\circ$ in the NH). The altitude of the warm/cold polar regions varies with time. Focusing on the SH, in the middle stratosphere (approximately 1 hPa), there is a rapid cooling of the pole during fall ($L_S = 38^\circ\text{--}50^\circ$), which leads to the formation of a very strong meridional temperature gradient near the pole (Figure 1(B)). As Titan nears the southern winter solstice ($L_S = 82^\circ\text{--}90^\circ$), the cooling expands from the pole to around 60°S and reduces the meridional temperature gradient slightly (Figure 1(C)). There is, however, a different evolution in the upper stratosphere (approximately 0.01 hPa), with an increase in temperature after the postfall equinox cooling, which expands and increases throughout fall (Figures 1(B)–(C)). This upper stratospheric cooling then warming is examined in detail in Teanby et al. (2017) and discussed further below.

In the model’s simulation of the temperature distribution, there is a warm bias, i.e., the simulated temperatures are generally larger than observations in the corresponding seasons (Figures 1(D)–(F)). This warm bias is largest in the upper levels of the model where it can be up to 30 K warmer than observations but decreases in magnitude toward the lower to middle stratosphere where it falls into better agreement. The exact cause of this bias is unknown, but possible causes include the imposed height of the model top (2×10^{-4} hPa), inaccuracies in the radiation scheme, or missing processes in the model. Despite this warm bias, however, the simulation qualitatively captures the key observed features discussed above. First, the model captures the appropriate timing for the transition of the cold pole from north to south during this time window (Figures 1(D)–(F)). As the cold pole transitions to the south, the model rapidly develops an intensified meridional temperature gradient in the lower stratosphere similar to that observed. This meridional temperature gradient then decreases in magnitude as the south pole approaches winter solstice, although one difference between the model and observations is that the vertical extent of cold air at the pole increases in the observations but decreases in the model.

By southern winter solstice (Figure 1(F)), the location of the warmest polar air in the model has shifted from 0.01 hPa to about 0.05 hPa. This change in the location of peak warm air over the pole is hinted at in the observations as well; however, the shift in the model is much larger. This discrepancy is most likely an artifact of the model top being too low compared to the likely vertical extent of motions; this constrains the flow within the model, resulting in the level at which there is no meridional temperature gradient at the pole being lower in altitude than observed.

We now consider the structure and evolution of the zonal-mean zonal wind, U . The winds inferred from CIRS observations during these three time periods show westerly winds in both hemispheres, with the strongest winds in the NH

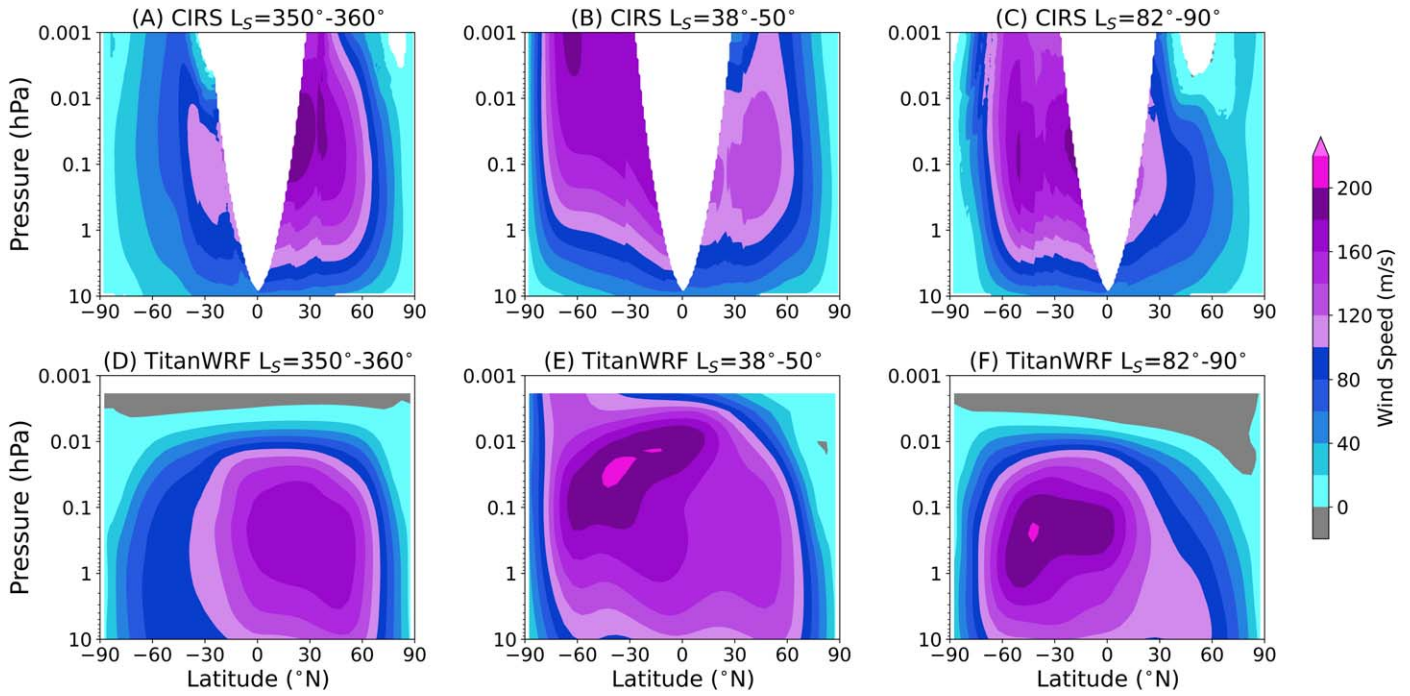


Figure 2. Zonally averaged zonal wind from CIRS (A–C) and TitanWRF (D–F) at southern fall equinox (left), southern midfall (middle), and southern winter solstice (right). Missing data in CIRS observations are due to the breakdown of gradient wind balance near the equator.

around southern autumnal equinox (Figure 2(A)) and in the SH during southern fall to winter (Figures 2(B) and (C)). Note that, as discussed in Section 2, U is calculated from the observed T assuming gradient wind balance and thus is not shown for the tropics. The maximum winds in the SH during fall ($L_S = 38^\circ\text{--}50^\circ$) occur in the mesosphere around 0.001 hPa at roughly 70°S and move down and equatorward to the upper stratosphere (0.1 hPa) and at 60°S by the winter solstice ($L_S = 82^\circ\text{--}90^\circ$). For all three periods shown, the maximum wind speed is roughly 200 m s^{-1} . This organized region of enhanced winds is known as a jet and defines the edge of the polar vortex.

There are again some clear model–data differences in the uppermost levels of the model ($<0.01\text{ hPa}$), with the model showing weaker winds that even switch to easterly in some places (Figures 2(D)–(F)). This discrepancy is likely tied to the imposition of the model top, as it acts as a rigid lid for the circulation within the model. Below 0.01 hPa, the model is in better agreement with CIRS observations. There is good agreement between the model and observations with regard to the meridional extent and magnitude of the SH jet. In agreement with observations, the strongest winds in the simulation ($\sim 200\text{ m/s}$) occur in fall during the formation of the south polar vortex, when the region of enhanced winds extends closer to the pole (Figure 2(E)). As observed, as Titan approaches SH winter solstice, the simulated peak winds decrease slightly with the peak wind region moving to lower altitudes and closer to the equator (Figure 2(F)).

Finally, we examine the PV distributions. In the PV derived from observations, the peak magnitude is at the south pole during the formation of the polar vortex in the fall ($L_S = 38^\circ\text{--}50^\circ$), corresponding to when wind speeds and temperature gradients are strongest (Figure 3(B)). Before and after this, however, the PV maximum is not located at the pole and instead sits about $10^\circ\text{--}20^\circ$ off the pole. This annular

structure of the PV is seen in the NH during spring and again in the SH during winter.

The model is generally in good agreement with the observed values of PV within the lower to middle stratosphere. PV decreases in the model between 0.1 hPa and 0.01 hPa due to the reduction in wind speeds at higher altitudes in the model, contrary to observations, but the latitudinal extent continues to be in agreement with observations. One key aspect that the model replicates well is the annular structure of PV observed in the mature stage of the polar vortex within the NH winter to spring as well as the SH winter (Figures 3(D) and (F)). At the 0.1 hPa level and above, the PV maximum sits $10^\circ\text{--}20^\circ$ off the pole, much like that observed.

4. Seasonal Evolution of the Polar Vortices as Seen in the Model Simulation

4.1. Annual Cycle of the Southern Polar Vortex

Having shown that the TitanWRF simulation captures the key features observed during the demise of the NH vortex and formation of the SH vortex in the Cassini observational period $L_S = 350^\circ\text{--}90^\circ$, we now examine the evolution of the simulated vortex over a complete annual cycle. We focus first on the SH vortex.

In the upper stratosphere (around 0.1 hPa) there is a nonmonotonic evolution of the simulated polar temperatures during the progression from SH fall to SH winter solstice (Figure 4(a)). The polar temperature during SH early fall ($L_S = 20^\circ$) cools rapidly, as anticipated by the reduction of solar heating as Titan approaches polar night at the south pole, but in SH late fall ($L_S = 50^\circ$), the cooling is reversed and the pole begins to warm, with this warming persisting until SH winter solstice ($L_S = 90^\circ$). As discussed above, this cooling and then warming also occurs in the Cassini CIRS observations (Teauby et al. 2019; Vinatier et al. 2020). Looking beyond the CIRS observational period, the simulation shows that these

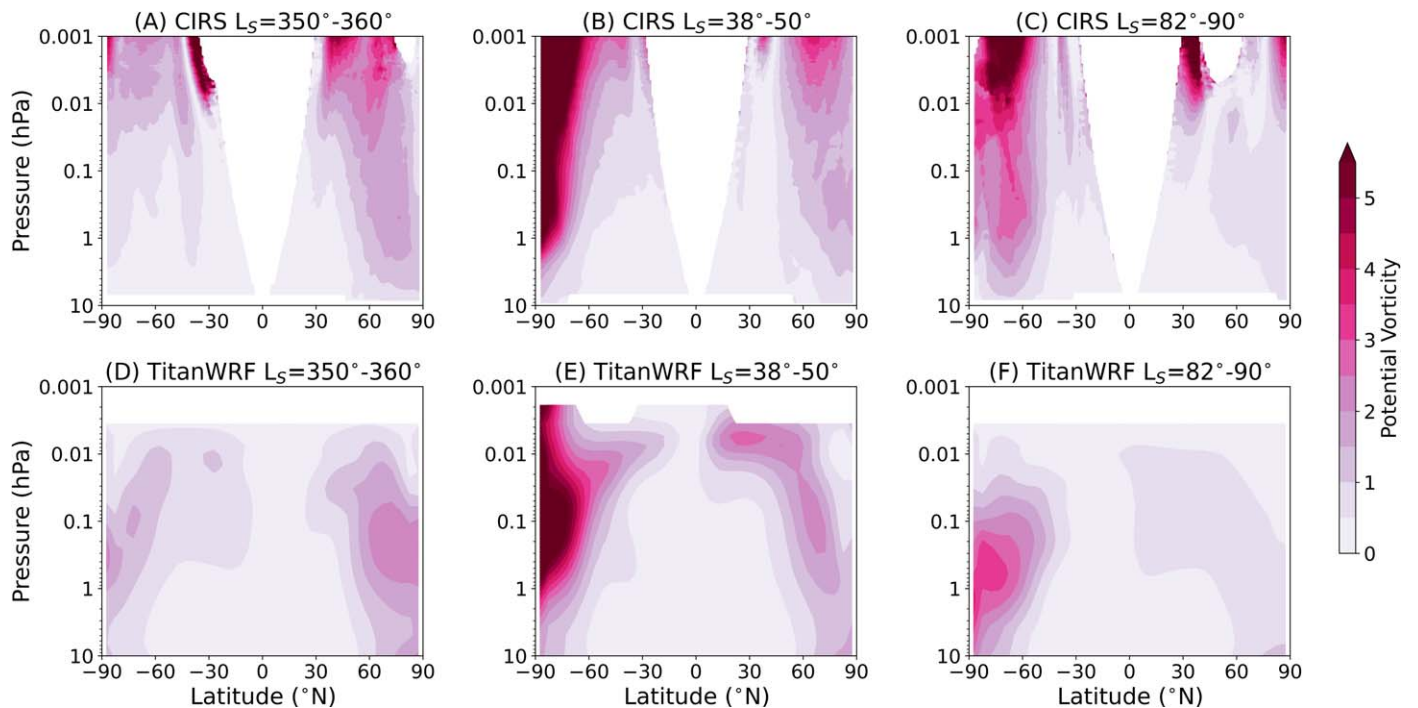


Figure 3. Zonally averaged absolute value of the scaled Ertel potential vorticity ($10^7 \text{ m}^2 \text{ s}^{-1} \text{ K kg}^{-1}$) from CIRS (A–C) and TitanWRF (D–F) at southern fall equinox (left), southern midfall (middle), and southern winter solstice (right). EPV values are first calculated on isentropic surfaces and then interpolated to pressure surfaces that can lead to the appearance of regions of undefined data in both observations and model output.

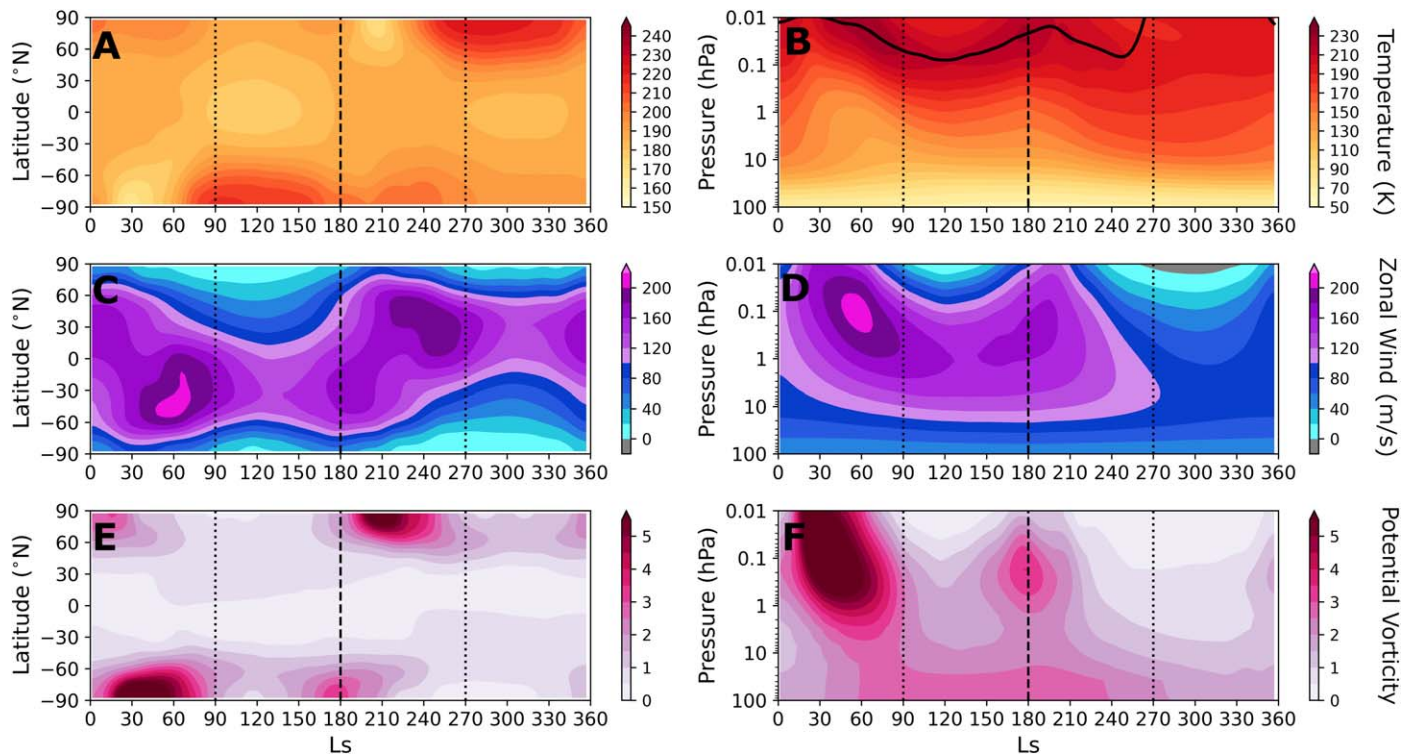


Figure 4. Contour plots of the zonal-mean T (K), U (m s^{-1}), and PV ($10^7 \text{ m}^2 \text{ s}^{-1} \text{ K kg}^{-1}$) for (a, c, e; left column) latitude vs. time on a fixed pressure surface (0.1 hPa) and (b, d, f; right column) pressure vs. time for averages over a latitude band ($70^\circ\text{--}90^\circ\text{S}$ for T and PV and $40^\circ\text{--}60^\circ\text{S}$ for U), for the whole year. Dotted lines represent the timing of solstices, dashed lines represent the timing of equinoxes, and the solid line in panel b depicts the stratopause, which lies above the plotted region in southern summer.

increased polar temperatures are sustained until SH late winter, but as the south pole approaches SH spring equinox, there is a brief period of secondary rapid cooling (around $L_S = 170^\circ$) before the return of a typical seasonal evolution trend. The

seasonal evolution varies with altitude, with the SH post-autumnal equinox cooling and then warming occurring later and having smaller amplitude at lower altitudes (Figure 4(b)). In the lower stratosphere (50–100 hPa), the fall warming does

not occur, and there is monotonic cooling from the SH fall equinox (~ 90 K at 50 hPa) to late SH winter (~ 75 K at 50 hPa) followed by a warming in SH spring (~ 85 K at 50 hPa). This pattern suggests that the warming signature is induced by the descent of air. As this air moves downwards, it warms due to adiabatic compression, increasing temperature within the descending air. This descent of warm air also results in a lowering of the polar stratopause (the point where the atmospheric temperature lapse rate flips from warming with height to reducing with height). In the lower stratosphere, there is little or no descent (and thus weaker or no adiabatic warming), resulting in cooling in the lower stratosphere throughout the SH fall–winter period.

Shifting the focus to zonal wind reveals a similar nonmonotonic behavior within the mid-to-upper stratosphere (Figures 4(c) and (d)). At 0.1 hPa in both hemispheres, the peak winds weaken and move equatorward during fall, reach their weakest values in midwinter, and then strengthen slightly and move back toward the pole just before each hemisphere’s respective spring equinox (Figure 4(c)). A similar seasonal evolution in the simulated winds around 0.1 hPa is evident in results from the LMD Titan model (see Figure 8(b) of Lebonnois et al. 2012). The restrengthening of the zonal winds around spring is due to the winter hemisphere pole cooling from a decrease in descending air causing less adiabatic compression/warming, which causes the meridional temperature gradient to be increased and drive stronger zonal winds. In terms of their vertical variation (Figure 4(d)), SH peak winds move down to around 1 hPa during fall, remain at this altitude in winter, and then move up in the atmosphere around the spring equinox.

There are accompanying changes in the PV: During both hemisphere’s fall, PV decreases at the pole, leading to the formation of an annulus with the latitude of the largest PV occurring off the pole at 70°S (Figure 4(e)). The region of peak PV also descends in altitude in the SH during the fall following the same vertical pattern seen in the temperature and winds (Figure 4(f)). As Titan approaches SH spring equinox, the peak PV moves back to the pole and increases in magnitude, providing another indication of the restrengthening of the polar vortex. After this brief restrengthening, there is a decrease in PV throughout the southern hemisphere (consistent with the weak temperature and wind gradients) as the polar vortex breaks down, followed by a transition into the summer weak flow.

4.2. Hemispheric Differences

The discussion above has focused on the evolution of the SH vortex, but a key question is whether the NH vortex has a similar evolution. If hemispheric symmetry is predicted by models, this supports combining Cassini observations from NH late winter to summer and SH late summer to winter solstice to give a more complete picture of the annual cycle of the polar vortices from observations, as was done in Sharkey et al. (2021). By contrast, if significant hemispheric asymmetry is predicted, then combining observations in this way is less well justified.

Examination of the left column of Figure 4 suggests a very similar evolution in the northern and southern hemispheres (when including a shift of 180° of L_S in the opposite hemisphere). To examine this similarity in evolution in more detail, we compare the average temperatures over each polar

region in the same seasons (at a few representative pressures) in Figure 5. There is a very similar evolution in the SH and NH, with both poles undergoing autumnal cooling followed by a winter warming, with a warm pole persisting until just before the spring equinox. Also, in both hemispheres, the reversal of polar cooling to warming occurs earlier in the fall at higher altitudes, i.e., the reversal occurs in the early fall at 0.1 hPa but in late fall at 1 hPa (Figures 5(A) and (B)). Although the evolution is similar, there are quantitative differences. First, the NH winter pole is warmer than the SH winter pole, whereas the NH summer pole is colder than the SH summer pole. Second, there is a slight difference between the timing of the reversal from cooling to warming during local winter, in that the NH seems to warm faster than the SH. This difference in the timing of warming is accompanied by higher temperatures during winter in the NH and then cooler temperatures in the summer due to the amount of time each hemisphere has to warm up/cool down.

These differences between the hemispheres are consistent with differences in insolation due to the eccentricity of the Saturn/Titan system around the Sun. Titan’s closest approach to the Sun (perihelion) occurs at $L_S = 277^\circ$, which is very close to the northern winter solstice ($L_S = 270^\circ$) and is when Titan receives the highest top of the atmosphere insolation ($\sim 16.8 \text{ W m}^{-2}$). Titan’s farthest point from the Sun along its orbit (aphelion) occurs at $L_S = 98^\circ$, just after the northern summer solstice ($L_S = 90^\circ$), when its top of the atmosphere solar radiation drops to a minimum ($\sim 13.5 \text{ W m}^{-2}$), representing about a 20% difference in insolation between the two orbital extremes. The timing of these events is consistent with the offset in temperature between the hemispheres during their respective seasons. During summer, changes in insolation directly impact the temperature by changing the shortwave radiative heating, meaning that southern polar latitudes in summer (around perihelion) are warmer than northern polar altitudes in summer (around aphelion). At polar latitudes in winter, changes in insolation influence the temperature indirectly via the global circulation, which impacts polar air descent and adiabatic warming. In NH winter, there is a stronger global circulation (due to the stronger solar forcing of SH summer upwelling motions near perihelion), which yields more descent and therefore greater adiabatic compression and warming over the north pole, while in the SH winter there is a weaker global circulation, which leaves the south pole colder than the NH winter pole.

Analysis of midlatitude zonal wind and polar PV (Figure 6) again shows a similar evolution in both hemispheres, with some relatively small quantitative differences. These differences can be tied to the previously noted temperature differences from Figure 5. During the fall, the NH polar temperatures increase faster than those in the SH, which leads to an earlier reversal of the polar temperature gradient and a slower maximum wind speed in the NH during vortex formation. As the SH pole continues to cool later into fall than the NH pole, there is also a delay in the time it takes for the SH pole to reach its maximum temperature during winter. This offset in the timing of polar warming means that the SH polar meridional temperature gradient supports increasing zonal winds for longer, which leads to a higher maximum zonal wind speed there. Both hemispheres come back into agreement during winter, when they both follow the previously described seasonal evolution.

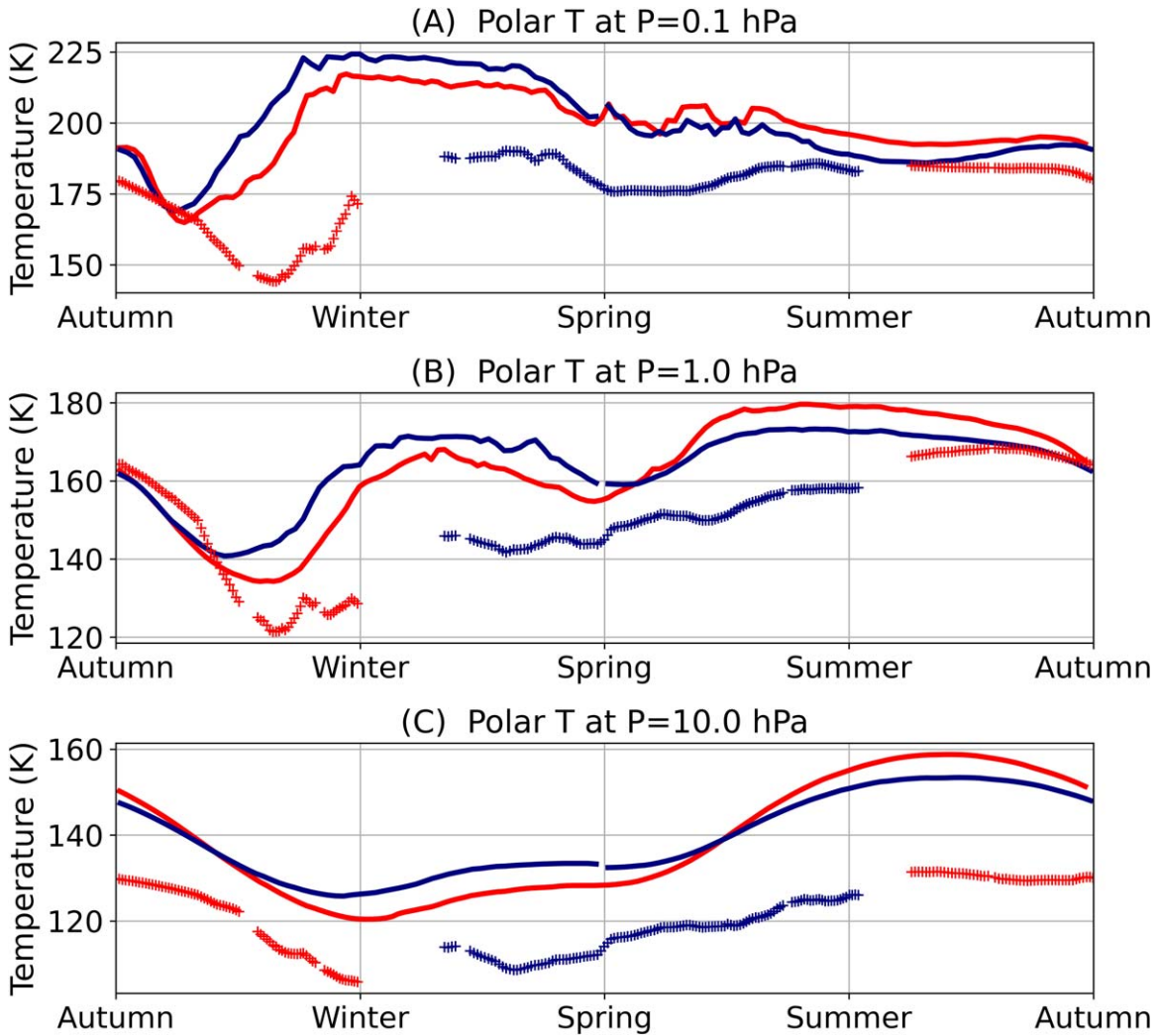


Figure 5. Annual evolution of polar temperature (70° – 90° average) for the northern (blue) and southern (red) hemispheres, at (a) 0.1. (b) 1, and (c) 10 hPa. TitanWRF is shown with solid curves and Cassini CIRS observations with crosses.

Polar PV is destroyed more rapidly in the NH during its fall due to the increased warming, while the SH polar PV is able to maintain higher values much later into its fall (Figure 6(b)). Both hemispheres reach a similar minimum value in midwinter, but the NH takes longer to increase PV around the spring equinox, while the SH starts to increase PV in late winter. Finally, both hemispheres have a similar timing for the reduction of PV during local summer.

As the hemispheric differences shown above are small and only from a single year, it is possible they could be due to interannual variability (generated by the inherently chaotic nature of the atmospheric dynamics) and not true hemispheric differences. To test this, we examined fields from a multiyear extension of this simulation and found that the annual evolution and hemispheric differences in temperature were consistent over multiple model years and that the annual variations and hemispheric differences were larger than differences between years (Figure 7). The extended multiannual TitanWRF simulation consistently showed both hemispheres undergoing this fall warming event every year, including the winter weakening of vortex strength and polar PV. The timing for the initialization of the fall warming event was the most variable aspect of the evolution, with the earliest event starting at $L_S = 30^{\circ}$ and the latest event starting at $L_S = 60^{\circ}$ in SH

($L_S = 210^{\circ}$ to $L_S = 240^{\circ}$ in NH), where the start of the event is qualitatively when the temperatures begin rising sharply in the polar regions. Once the poles have warmed up, however, the spread in temperatures between years becomes very narrow, with the largest spread being ~ 5 K during the winter warm period ($L_S = 90^{\circ}$ – 170° SH, and $L_S = 270^{\circ}$ – 350° NH). Similarly, the spread in midlatitude winds is very small between years, with the largest spread being ~ 20 m s^{-1} right before the winter weakening ($L_S = 80^{\circ}$ SH, and $L_S = 260^{\circ}$ NH) due to small differences in the timing of the weakening, and then narrowing to ~ 10 m s^{-1} during the weakening. Because these differences between years are small and the overall yearly evolution is the same, we conclude that the hemispheric differences are not an expression of interannual variability and are instead a feature of the polar vortex evolution.

5. Mechanisms

Our analysis suggests that subsidence of warm air from aloft is the cause of the winter weakening of the polar vortex. To explore this in more detail, we examine the MMC and the rate of subsidence over the winter pole. Over the Titan year, the MMC oscillates between two modes: a mode with a single cell from the summer to winter pole (e.g., Figures 8(B)–(E)) and a

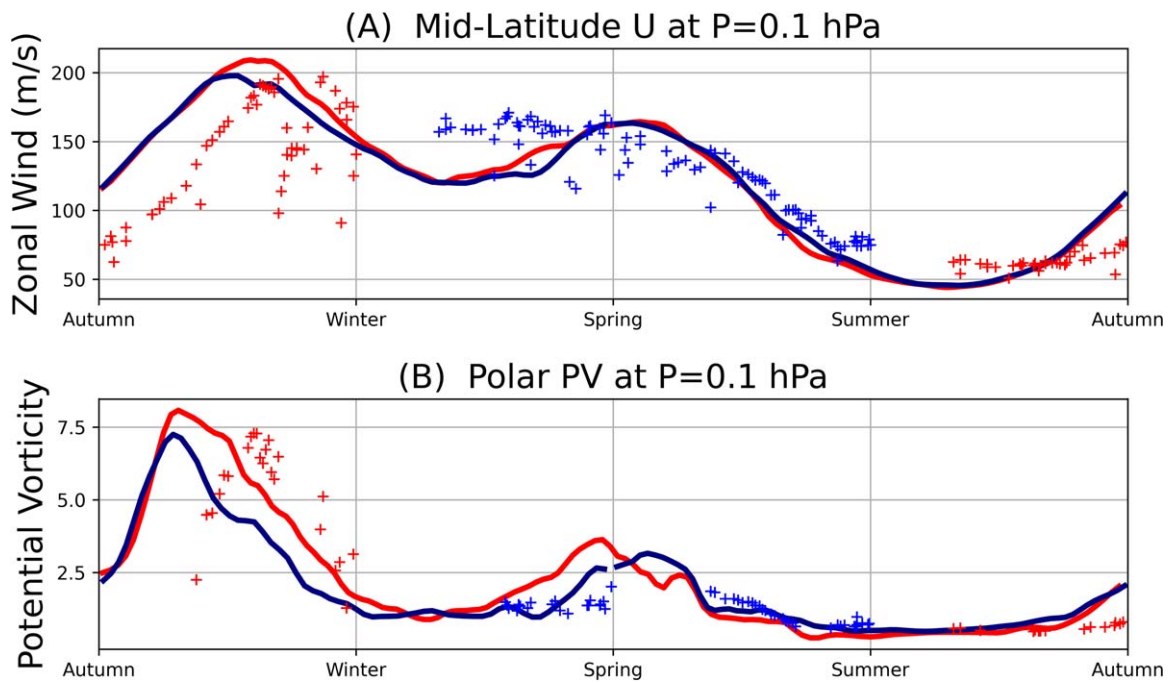


Figure 6. Annual evolution of zonally averaged U (m s^{-1}) averaged between 40° – 60° north (blue) and south (red) (a), and PV ($10^7 \text{ m}^2 \text{ s}^{-1} \text{ K kg}^{-1}$) averaged between 70° – 90° north (blue) and south (red) (b) shown for a full year at the 0.1 hPa pressure level. TitanWRF is shown with solid curves and Cassini CIRS observations with crosses.

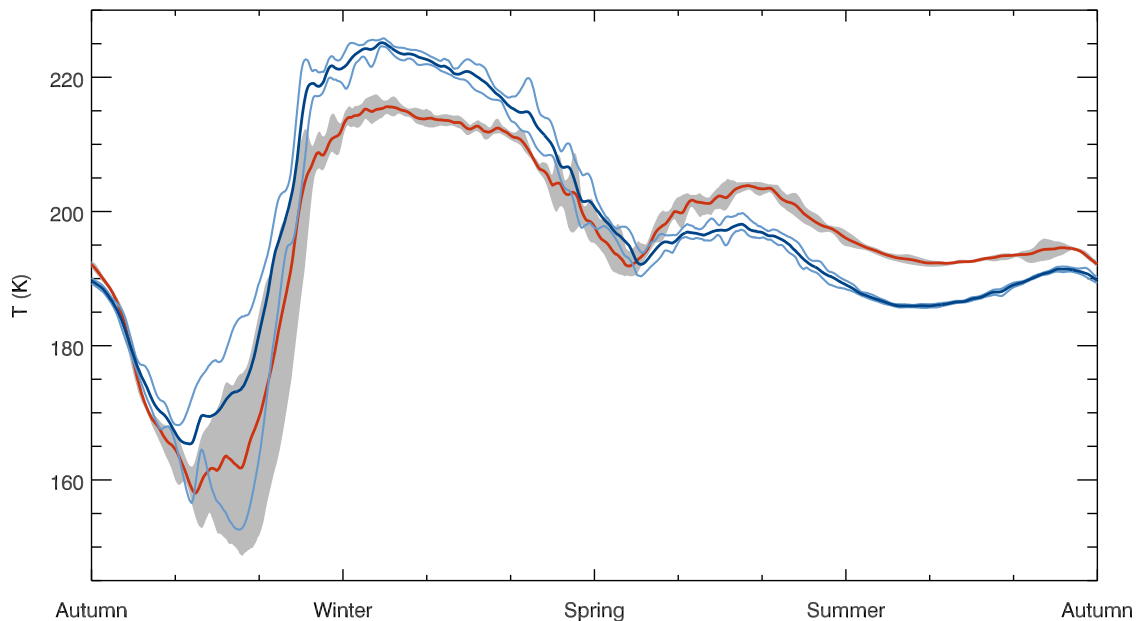


Figure 7. Annual evolution of the polar temperature (70° – 90° average) for the northern (blue) and southern (red) hemispheres, at 0.1 hPa from a multiyear extension of the TitanWRF simulation (additional four years). Thick lines represent the four-year average; the shaded region (SH) and thin blue lines (NH) represent the maximum and minimum temperatures over the four years.

double-cell mode around the equinoxes with flow from the tropics to pole in each hemisphere (e.g., Figures 8(A) and (F)). The duration of the two-cell mode ($\sim 60^{\circ}$ of L_S) is much shorter than that of the single-cell model ($\sim 120^{\circ}$ of L_S).

During single-cell periods (Figures 8(B)–(E)), there is ascent at the summer pole and strong descent at the winter pole. During this time there are strong zonal winds at the winter edge of the cell (see Figure 2), consistent with the conservation of angular momentum within the upper branches of the cell. The winter polar subsidence acts to adiabatically compress and

warm air as it descends over the winter pole. This warming is largely balanced by radiative processes (sum of longwave cooling and shortwave heating) but there is residual net warming that leads to the peak temperature just around winter solstice when subsidence reaches its maximum sustained value (Figure 8(D)). As Titan approaches the equinoxes, the single-cell structure breaks down and splits into two counterrotating cells (Figures 8(A) and (F)). This breakdown reduces the subsidence and accompanying adiabatic heating occurring over the (previously winter) pole, causing the secondary

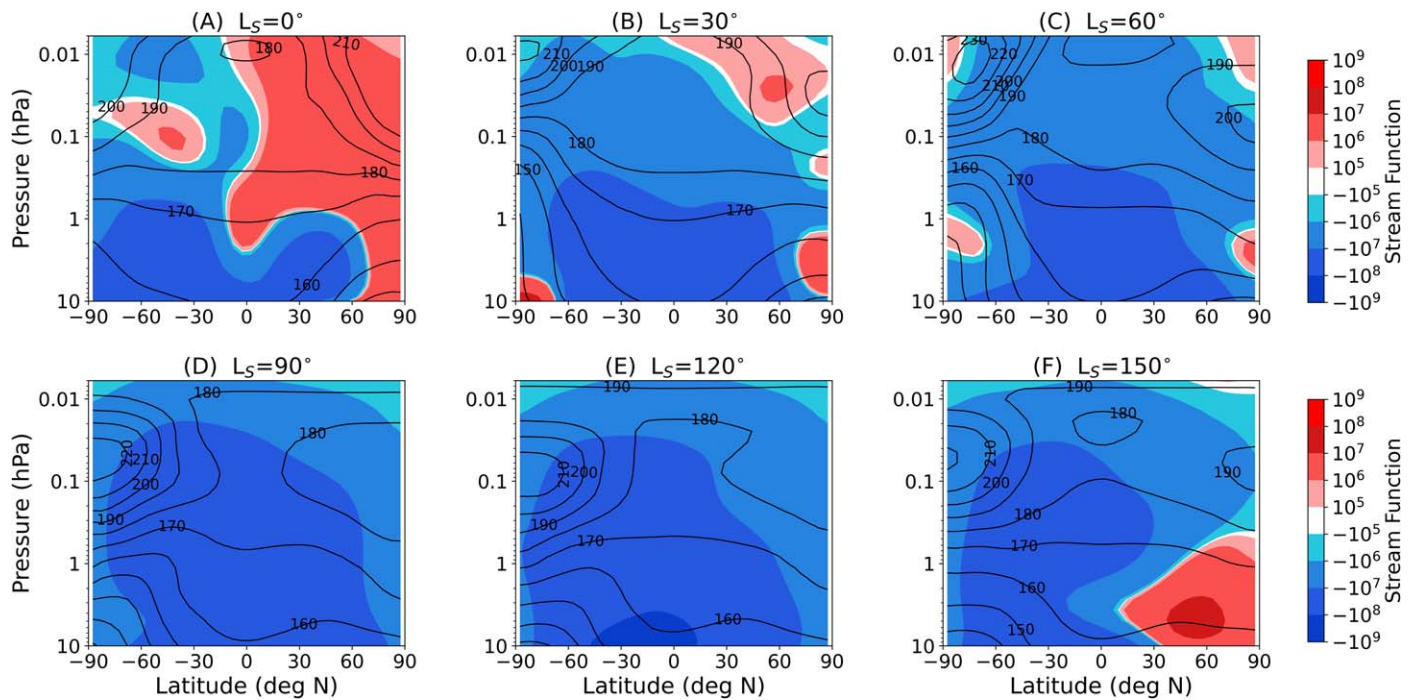


Figure 8. TitanWRF pairs of T (K) contours and MMC ($\text{kg m}^{-1} \text{s}^{-1}$) color shading (positive values indicate clockwise rotation) shown from southern fall equinox to late southern winter.

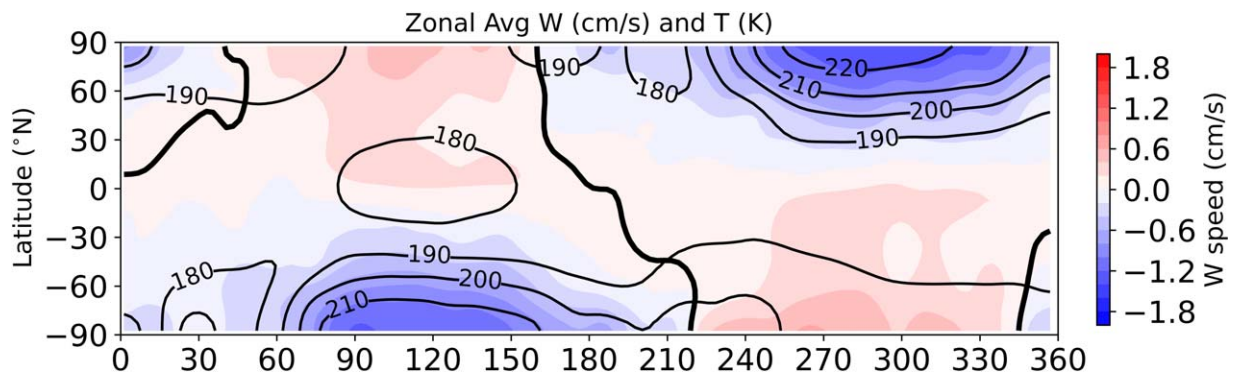


Figure 9. Vertical velocity (cm s^{-1} , color fill) and temperature (K, contour lines) as a function of solar longitude and latitude on a 0.1 hPa constant pressure surface from the TitanWRF simulation. The thick black line represents the location of the zero value of the stream function at this pressure.

restrengthening of the polar vortex to occur as temperatures cool slightly. Eventually, the subsidence is cut off and the polar vortex dies as the MMC transitions to a single cell toward the opposite hemisphere.

The seasonality in the polar subsidence and relationship with temperature discussed above can also be seen in Figure 9, which shows the seasonal variation of vertical velocity (shading) and temperature (contours) at 0.1 hPa in the TitanWRF simulation. Focusing on the SH for simplicity, during the first half of fall ($L_S = 0^\circ$ – 50°), there is a very weak subsidence over the pole and temperatures decrease as the pole approaches polar night. Descent increases around $L_S = 50^\circ$ and at the same time temperatures begin to rise at the pole until they hit a maximum at the winter solstice ($L_S = 90^\circ$), at which time the descent also reaches its maximum. The descent is sustained until about $L_S = 160^\circ$, at which time MMC transitions into a double cell, and the polar descent rate decreases, and the polar temperatures begin to drop at a significantly faster rate. Around $L_S = 220^\circ$, the MMC transitions to a single-cell circulation, with upwelling in the southern (summer) hemisphere and a

warming south pole. Idealized general circulation model simulations show midwinter weakening of the polar vortex similar to that described above, for sufficiently slow rotation rates (Guendelman et al. 2022). In these simulations, as in TitanWRF, the midwinter MMC extends from the summer to winter poles, and the descending motion around the winter pole results in weak meridional temperature gradients and a weaker polar vortex.

As shown in Figure 4(d), there is a large seasonal variation in the height of the peak winds. This is consistent with the seasonal changes in the meridional temperature gradient and thermal wind balance. During fall and winter in the SH, there is a negative meridional temperature gradient (from south to north) in the upper stratosphere, which implies a decrease in the zonal wind with height, whereas in the lower stratosphere there is a positive temperature gradient and an increase in winds with height. This means that the maximum wind speed occurs between these regions where there are weak meridional temperature gradients. As shown in Figure 8, the position of this inflection point in the meridional temperature gradient

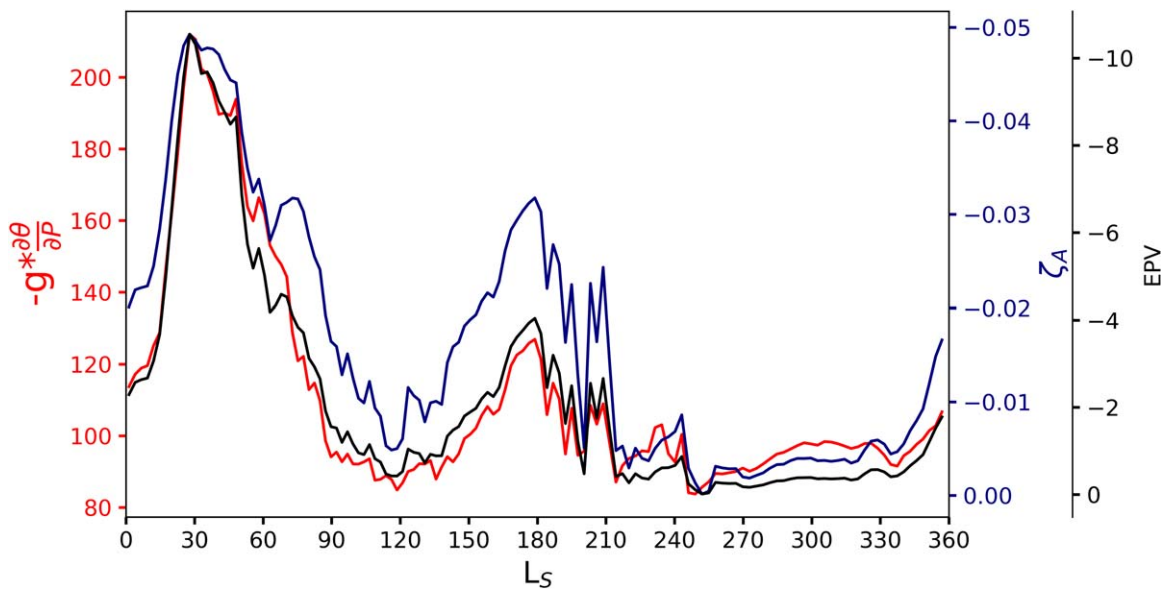


Figure 10. Evolution of zonal-averaged PV ($10^7 \text{ m}^2 \text{ s}^{-1} \text{ K kg}^{-1}$) in black, static stability $-g \frac{\partial \theta}{\partial p}$ ($\text{K m}^2/\text{kg}$) in red, and absolute vorticity ζ_A (s^{-1}) in blue, throughout the year averaged over 80° – 90°S on a 0.1 hPa surface.

moves from around 0.08 hPa at $L_S = 30^\circ$ (Figure 8(B)) down to around 1 hPa at $L_S = 120^\circ$ (Figure 8(E)), and then moves slightly back up to 0.5 hPa by $L_S = 150^\circ$ (Figure 8(F)). A similar vertical variation occurs in the maximum wind speed, see Figure 4(d).

Both observations and model output show vortices with an annular PV structure (maximum PV located away from the pole). This occurs during late fall and winter when there is strong descent over the pole and an increase in polar temperatures. For an annulus to form, there has to be local reduction of PV at the pole. Referring back to Equation (1) for the definition of PV, this can happen by decreasing static stability ($-g \frac{\partial \theta}{\partial p}$) and/or absolute vorticity (via decreases in the relative vorticity) in polar regions. Harvey et al. (2009) investigated a similar annular feature in Earth’s mesosphere and proposed that the reduction of static stability, via downward motion of warm air, is the primary driver for the creation of an annulus of PV. Consistent with this, examination of polar static stability in the TitanWRF simulation shows a decrease during the period of strong descent in fall, and the temporal variation in static stability matches that of the PV, i.e., they both reach a maximum value around $L_S = 30^\circ$ in the SH and then rapidly decrease in magnitude until $L_S = 120^\circ$ where they both reach a minimum, before increasing in magnitude to a secondary peak at $L_S = 180^\circ$ (Figure 10). However, there are also changes in the horizontal temperature gradient with accompanying changes in the zonal winds, and these changes could result in decreased PV in polar regions through a decrease in relative vorticity. Indeed, examination of polar absolute vorticity shows the same evolution as static stability and PV (Figure 10). The adiabatic compressive heating of descending air changes both the static stability ($-g \frac{\partial \theta}{\partial p}$) and the pole-to-equator temperature gradient, which, via thermal wind balance, changes the absolute vorticity ($\zeta_A = \mathbf{f} + \zeta(\theta)$), and changes in both static stability and vorticity contribute to the formation of annular PV.

6. Conclusions

Analysis of a TitanWRF simulation has revealed a nonmonotonic behavior of Titan’s wintertime polar vortices, with a clear minimum in polar vortex strength between winter solstice and spring equinox. The polar middle-upper stratosphere cools after fall equinox, then rapidly warms in mid-late fall to reach a maximum around the winter solstice, which is sustained until just before the spring equinox when there is a brief secondary cooling period. Accompanying these temperature changes is a strengthening of the westerly jet speeds and polar PV after the fall equinox, then a weakening from mid-late fall through winter, with secondary strengthening around the spring equinox before the decay of the vortex in summer.

The seasonal evolution of the polar vortices is similar in the two hemispheres, with only small quantitative differences that can be related to Titan’s orbital eccentricity (perihelion occurs around the NH winter solstice and aphelion around the SH winter solstice). The NH summer pole is slightly colder than the SH summer pole due to the reduced insolation. Conversely, the NH winter pole is slightly warmer than the SH winter pole due to the combined effect of the relatively larger insolation at the NH winter hemisphere compared to the SH winter hemisphere and a relatively stronger mean meridional circulation in the southern summer (northern winter) perihelion season compared to the northern summer (southern winter) aphelion season, leading to increased adiabatic warming in the northern winter compared to southern winter. These hemispheric differences are much smaller than the seasonal variations, and differences between observations of the NH vortex in late northern winter and the SH vortex in early winter are likely due to the different seasonality of the observations rather than fundamental hemispheric differences in the polar vortices. Furthermore, the comparative smallness of the hemispheric differences suggests it is reasonable to combine Cassini observations from the two hemispheres to form a more “complete” view of the annual cycle of the polar vortices (e.g., as done in Sharkey et al. 2021).

Both observations (Sharkey et al. 2021) and TitanWRF results show an annular PV structure during late fall–winter, with lower PV at the pole than in a broad latitudinal region centered at about 10° – 30° from the pole. This annular structure occurs during the period of strong polar descent (and adiabatic warming), suggesting this is the cause of the annular structure. As occurs in Earth’s mesosphere (Harvey et al. 2009), the descent causes a reduction in static stability at the pole, which then lowers PV at the pole relative to lower latitudes and leads to the development of an annulus of PV. However, there is also a decrease in polar relative vorticity (from the reduced meridional temperature gradients and zonal winds accompanying the polar descent), and reductions in both static stability and relative vorticity contribute to the decrease in polar PV.

The analysis in this paper has considered only the variations in zonal-mean fields because the three-dimensional fields from the TitanWRF simulation only show very weak zonal variations. For example, the standard deviation of the longitudinal variation of temperature is generally less than 0.1% of the zonal mean. Analysis of CIRS temperature and trace gas measurements also show limited zonal variations. In the observations, the stratospheric symmetry axis is tilted from the solid-body rotation axis by around 3° – 4° (e.g., Achterberg et al. 2008; Sharkey et al. 2020), which is not captured by the model. However, when this is removed, there are insignificant zonal variations (e.g., Sharkey et al. 2020) that are smaller in magnitude than the retrieved temperature uncertainty. In the model, there are limited zonal variations throughout the Titan year, including during the winter weakening and the summer decay of the polar vortex. This is a stark contrast to Earth’s stratospheric polar vortices, which are very distorted during midwinter weakening and the end of winter breakup.

While the simulation reproduces the key observed features of the polar vortex evolution, there is a substantial bias in the simulated temperatures in the upper stratosphere/mesosphere. This is likely due to the imposed height of the model top (2×10^{-4} hPa), which prevents a full representation of the circulation that would otherwise develop into the mesosphere. By increasing the model top height, the interface between the stratosphere and mesosphere should be more accurately represented, allowing for a more realistic simulation of the general circulation of Titan’s atmosphere and temperature field. Another source of bias could be inaccuracies in predictions of heating rates in the radiation scheme. Future work will examine the sensitivity of the simulations to these aspects and adjust model parameters to improve the accuracy of the simulations where needed. A more accurate representation of the temperature and circulation will also facilitate better analysis of the characteristics of, and relationships in, Titan’s atmosphere. For example, future work will investigate the dynamic coupling between stratospheric superrotation and the polar vortex.


Now that we have an understanding of how the polar vortex evolves over the span of a Titan year from the simulation, another area of future work is examining the transport of tracers within the model. The observed distributions of photochemical trace gases with mesospheric sources have been linked to transport associated with the polar vortices, i.e., the transport of gases from the mesosphere into and down through the

stratosphere within the polar vortices, and the reduced exchange between polar and midlatitudes because of the polar vortex edge. However, it is difficult to quantify this transport from available trace gas observations, and there is again a lack of observations during the middle of winter when the weakening of the vortex is predicted. Thus, it is unknown how the vertical and horizontal transport varies through the polar vortex lifecycle. We plan to include tracers in future simulations in order to quantify this transport. Acknowledgments

The authors acknowledge NASA Solar System Workings grant 80NSSC20K0138 for funding support to accomplish this work. A. Toigo also thanks the Johns Hopkins University Applied Physics Laboratory Lawrence R. Hafstad Sabbatical Fellowship for additional funding support for this project. N. A. Teanby and J. Sharkey are funded by the UK Science and Technology Facilities Council. The TitanWRF output is available at <https://data.nas.nasa.gov/titangcm/> and the Sharkey et al. (2021) CIRS results are available at <https://data.mendeley.com/datasets/wn8j8f8ck7/1>.

ORCID iDs

J. Shultis  <https://orcid.org/0000-0002-8657-2872>

N. A. Teanby  <https://orcid.org/0000-0003-3108-5775>

References

- Achterberg, R. K., Conrath, B. J., Gierasch, P. J., Flasar, F. M., & Nixon, C. A. 2008, *Icar*, 194, 263
- Achterberg, R. K., Gierasch, P. J., Conrath, B. J., Flasar, F. M., & Nixon, C. A. 2011, *Icar*, 211, 686
- Anderson, C. M., Samuelson, R. E., & Nna-Mvondo, D. 2018, *SSRv*, 214, 125
- Cordiner, M., Garcia, E., Cosentino, R., Teanby, N., & Nixon, C. 2020, *EPSC*, 14, EPSC2020-424
- Coustenis, A., Jennings, D. E., Achterberg, R. K., et al. 2018, *ApJ*, 854, L30
- Flasar, F. M., & Achterberg, R. K. 2009, *RSPTA*, 367, 649
- Guendelman, I., Waugh, D. W., & Kaspi, Y. 2022, *PSJ*, in press
- Harvey, V. L., Randall, C. E., & Hitchman, M. H. 2009, *JGRD*, 114, D22105
- Hong, S.-Y., & Pan, H.-L. 1996, *MWRv*, 124, 2322
- Le Mouélic, S., Rodríguez, S., Robidel, R., et al. 2018, *Icar*, 311, 371
- Lebonnois, S., Burgalat, J., Rannou, P., & Charnay, B. 2012, *Icar*, 218, 707
- Lellouch, E., Gurwell, M. A., Moreno, R., et al. 2019, *NatAs*, 3, 614
- Lora, J. M., Lunine, J. I., & Russell, J. L. 2015, *Icar*, 250, 516
- Mathé, C., Vinatier, S., Bézard, B., et al. 2020, *Icar*, 344, 113547
- McKay, C. P., Pollack, J. B., & Courtin, R. 1989, *Icar*, 80, 23
- Newman, C. E., Lee, C., Lian, Y., Richardson, M. I., & Toigo, A. D. 2011, *Icar*, 213, 636
- Newman, C. E., Richardson, M. I., Lian, Y., & Lee, C. 2016, *Icar*, 267, 106
- Plumb, R. A., Heres, W., Neu, J. L., et al. 2002, *JGRD*, 108, 8309
- Richardson, M. I., Toigo, A. D., & Newman, C. E. 2007, *JGRE*, 112, E09001
- Sharkey, J., Teanby, N. A., Sylvestre, M., et al. 2020, *Icar*, 337, 113441
- Sharkey, J., Teanby, N. A., Sylvestre, M., et al. 2021, *Icar*, 354, 114030
- Sylvestre, M., Teanby, N. A., Vinatier, S., Lebonnois, S., & Irwin, P. G. J. 2018, *A&A*, 609, A64
- Sylvestre, M., Teanby, N. A., Vatan d’Ollone, J., et al. 2020, *Icar*, 344, 113188
- Teanby, N. A., de Kok, R., Irwin, P. G. J., et al. 2008, *JGRE*, 113, E12003
- Teanby, N. A., Sylvestre, M., Sharkey, J., et al. 2019, *GeoRL*, 46, 3079
- Teanby, N. A., Bézard, B., Vinatier, S., et al. 2017, *NatCo*, 8, 1586
- Tritscher, I., Pitts, M. C., Poole, L. R., et al. 2021, *RvGeo*, 59, 1
- Vinatier, S., Mathé, C., Bézard, B., et al. 2020, *A&A*, 641, A116
- Vinatier, S., Bézard, B., Lebonnois, S., et al. 2015, *Icar*, 250, 95
- Vinatier, S., Bézard, B., Nixon, C. A., et al. 2010, *Icar*, 205, 559
- West, R. A., Del Genio, A. D., Barbara, J. M., et al. 2016, *Icar*, 270, 399